

Magneto-optical absorption in semiconducting spherical quantum dots: Influence of the dot-size, confining potential, and magnetic field

Manvir S. Kushwaha

Department of Physics and Astronomy, Rice University,

P.O. Box 1892, Houston, TX 77251, USA

(Dated: May 11, 2019)

Abstract

Semiconducting quantum dots – more fancifully dubbed artificial atoms – are quasi-zero dimensional, tiny, man-made systems with charge carriers *completely* confined in all three dimensions. The scientific quest behind the synthesis of quantum dots is to create and control future electronic and optical nanostructures engineered through tailoring size, shape, and composition. The *complete* confinement – or the lack of any degree of freedom for the electrons (and/or holes) – in quantum dots limits the exploration of *spatially localized* elementary excitations such as plasmons to *direct* rather than *reciprocal* space. Here we embark on a thorough investigation of the magneto-optical absorption in semiconducting *spherical* quantum dots characterized by a confining harmonic potential and an applied magnetic field in the symmetric gauge. This is done within the framework of Bohm-Pines' random-phase approximation that enables us to derive and discuss the full Dyson equation that takes proper account of the Coulomb interactions. As an application of our theoretical strategy, we compute various single-particle and many-particle phenomena such as the Fock-Darwin spectrum; Fermi energy; magneto-optical transitions; probability distribution; and the magneto-optical absorption in the quantum dots. It is observed that the role of an applied magnetic field on the absorption spectrum is comparable to that of a confining potential. Increasing (decreasing) the strength of the magnetic field or the confining potential is found to be analogous to shrinking (expanding) the size of the quantum dots: resulting into a blue (red) shift in the absorption spectrum. The Fermi energy diminishes with both increasing magnetic-field and dot-size; and exhibits saw-tooth-like oscillations at large values of field or dot-size. Unlike laterally confined quantum dots, both (upper and lower) magneto-optical transitions survive even in the extreme instances. However, the intra-Landau level transitions are seen to be forbidden. The spherical quantum dots have an edge over the strictly two-dimensional quantum dots in that the additional (magnetic) quantum number makes the physics richer (but complex). A deeper grasp of the Coulomb blockade, quantum coherence, and entanglement can lead to a better insight into promising applications involving lasers, detectors, storage devices, and quantum computing.

PACS numbers: 73.21.La; 78.67.Hc; 81.07.Ta; 85.70.Sq

I. INTRODUCTION

The past two decades have seen very intense research efforts on the band-gap engineering in the synthetic semiconducting systems. Thanks to the development of epitaxial-growth technology and electron lithography, this field has created an excellent example of how the fundamental science and technology can interact and influence one another. We refer, in particular, to the exotic physics emerging from the semiconducting quasi- N -dimensional electron systems (QNDES); with N [$\equiv 2, 1, \text{ or } 0$] being the degree of freedom. While the seeds of the QNDES were sown much earlier [1], the discovery of quantum Hall effects is known to have induced the titanic research interest to see the consequent changes with diminishing system's dimensions from 3 to 2, 2 to 1, and 1 to 0. These are becoming known as quantum wells, quantum wires, and quantum dots in which the charge carriers exposed to electric and/or magnetic fields can [and do] reveal novel quantal effects that strongly modify the behavior characteristics of the resulting devices. The urge for such miniaturization lies in the current quest for potentially *smaller* and *faster* devices. A comprehensive review of the electronic, optical, and transport phenomena in the quantum structures of reduced dimensionality can be found in Ref. [2].

What makes these QNDES so much attractive are the smaller effective masses of the charge carriers and (substantially) large (background) dielectric constants. As a result, the charge carriers in semiconductors are more responsive to minute compositional changes or small perturbations – a situation that is exploited for device applications and for making model systems unattainable with free particles. The quantum size effects arise when the dimensions of a system become comparable to the de-Broglie wavelength [$\lambda \sim 10$ nm]. These are the crucial factors that spurred the fabrication of quantum wells, wires, and dots with the same fundamental principle: confine the electrons in a semiconductor with a smaller band-gap sandwiched between two identical semiconductors with a larger band-gap – a measure of the amount of energy needed to be pumped into the material to get electrons flowing. Thus an ultra thin layer with free charge carriers forms the Q2D quantum well; a narrow strip sliced from the Q2D layer makes a Q1D quantum wire; and dicing up a Q1D wire yields Q0D quantum dot.

By controlling the size and dimensions of such QNDES, researchers can tailor the electronic, optical, and transport properties of a device at will. In theory, the fewer the dimension, the finer the tuning, the sharper the clustering of energy states around specific peaks, and more important the many-body effects. In addition, the reduced degrees of freedom allow detailed and often exact calculations. The condensed matter physicists still fondly remember the excitement that followed the original proposals for designing the quantum wells [3], quantum wires [4], and quantum dots [5]. If recent history (of past 20 years) is any guide, it may not be an exaggeration to state that the vast majority of the condensed matter physicists – theorists and experimentalists – are still overwhelmingly fascinated by these low-

dimensional, quantum structures. It seems to be true no matter if they name it the spintronics, topological insulators, graphene, silicene, or germanene. The ability of these nanostructures to turn the broad energy bands of the parent semiconductors into sharply defined energy levels is a transformation that promises greater speed and efficiency for the resulting electronic and optical devices.

Ever increasing interest in these quantum structures is ascribed not only to their potential applications but also to the fundamental physics involved [2]. For instance, the Q2DES (or quantum wells and superlattices) allow the researchers a crystal clear observation of the Bloch oscillations, unobservable in the conventional solids. The Q1DES (or quantum wires and lateral superlattices) offer us an excellent, unique opportunity to study the real 1D Fermi gases in a relatively controlled manner. The Q0DES (or quantum dots or antidots) allow us a testing ground for studying the electron-electron interactions in a, neat and clean, tiny laboratory within the so-called artificial atoms.

Scientists have approached the fabrication of quantum dots from two very different points of view: (i) a top-down approach in which the extent and dimensionality of the solid has gradually been reduced, and (ii) a bottom-up in which quantum dots are viewed as extremely large molecules or colloids. The quantum dots grown by epitaxial and lithographic techniques are in the size regime from 1 μm down to 10 nm, whereas the colloidal samples vary in diameter from the truly molecular regime of 1 nm to about 20 nm. The latter systems are also known in the literature by the names of colloidal quantum dots or nanocrystals. The spherical quantum dots (SQDs), which are the subject matter of the present work, are precisely the systems that belong to this family of systems and are playing better responsive role as lasers than their epitaxial-cum-lithographic counterparts.

The research interest burgeoned in SQDs has focused mostly on the excitonic aspects of the bulk part with the surface states, generally, eliminated by enclosure in a material of larger band-gap [6-35]. Existing research work has devoted to understanding diverse fundamental properties of SQDs related with the exciton dynamics. These include the distribution of electrons and holes, exciton formation, exciton binding energy, exciton absorption, recombination, impact ionization, carrier multiplication, direct and indirect transitions, exciton spin dynamics, optical non-linearity, oscillator strength, and excitonic atoms – to name a few – in the theoretical [6-14, 17, 19, 21-22, 24-28, 30-35] and experimental [15, 16, 18, 20, 23, 29] works. Theoretical models employed for this purpose involve the tight-binding, effective-mass approximation, variational approach, perturbative scheme, finite-element, pseudopotential, and the Kane's $\mathbf{k} \cdot \mathbf{p}$ model in the systems of CdS, CdSe, PbTe/CdTe, and InAs/GaAs; and considering the effect of an applied magnetic field [13, 17, 19-21, 34], the temperature dependence [23], the phonon effects [25], the Coulomb impurities [30], and the surface effect [32].

Singular in the list of references is the Ref. 35 in which the authors have studied the SQDs made up of 3D topological insulator (TI) materials, such as PbTe/Pb_{1-x}Sn_xTe, with bound massless and helical

Weyl states existing at the interface. The authors demonstrate a complete confinement of the massless Weyl fermions at the interface and identify the spin locking and the Kramers degeneracy, the hallmarks of a 3D TI. They argue that the semiclassical Faraday effect [due to the Pauli exclusion principle] can be used to read out spin quantum memory in the optically mediated quantum computing. It is captivating given the ongoing excitement behind the quantum computation and the advocacy of comparing the electronic, spintronic, and optical processing of information.

The scrutiny of the existing literature on the spherical quantum dots reveals the lack of genuine efforts devoted to theorizing the magneto-optical absorption that generally justifies the (localized) plasmon excitation peaks observed in the optical experiments. The present paper is motivated to fill that gap. We consider a SQD characterized by a confining harmonic potential and an applied magnetic field in the symmetry gauge. We believe that the harmonic potential confining the SQDs is the most reasonable approximation justifiable for the situation when the number of electrons (N) in the dots is small. This model of harmonic potential validates the Kohn's theorem [36] – generalized to Q0DES [37] – which states that the FIR resonant spectrum of a correlated many-electron system is insensitive to the interaction effects. Identical physical conditions (of confinement and magnetic field) yield consistent results even in relatively more sophisticated (spintronic) QNDES [38-40].

As such, we employ the Bohm-Pines' full-fledged random-phase approximation (RPA) [41] and derive the total [or interacting] density-density correlation function (DDCF) in terms of the Dyson equation that takes proper account of the Coulomb interactions. To this end, we make use of the eigenfunctions and eigenenergies obtained as the solutions of the relevant Schrodinger equation in the spherical geometry. As an application of the analytical results, we compute the Fock-Darwin spectrum [42-44], the magneto-optical absorption, the Fermi energy, and the Radial distribution for electrons. The finiteness of the SQD is accounted for by matching a proper boundary condition: the total eigenfunction vanishes at the surface of the quantum dot. In the illustrative examples we stress upon the dependence on the dot-size, the confining potential, and the magnetic field.

The rest of the paper is organized as follows. In Sec. II, we discuss the theoretical framework within the RPA that allows us to derive the total DDCF in terms of the Dyson equation embodying properly the Coulomb interactions, to devise the selection rules for the magneto-optical transitions, to compute the Fermi energy, and to discuss the radial distribution of electrons. In Sec. III, we discuss several illustrative examples of, e.g., the Fock-Darwin spectrum, Fermi energy, magneto-optical absorption, optical transitions, and radial distribution of electrons. Finally, we conclude our findings and suggest a few interesting features worth adding to the problem in Sec. IV.

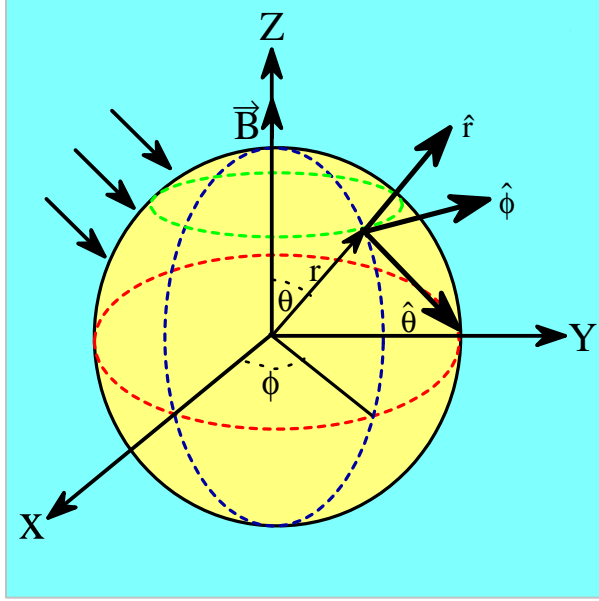


FIG. 1: (Color online) The schematics of the spherical geometry with coordinates (r, θ, ϕ) : Here r , θ , and ϕ are, respectively, the radial coordinate, the polar angle, and the azimuthal angle. The confinement potential $V(\mathbf{r}) = \frac{1}{2} m^* \omega_o^2 r^2$; and the magnetic field in the symmetric gauge is defined by the vector potential $\mathbf{A}(\mathbf{r}) = \frac{1}{2} (\mathbf{B} \times \mathbf{r})$.

II. THEORETICAL FRAMEWORK

A. Eigenfunction and eigenenergy

We consider a quasi-zero dimensional electron system three-dimensionally confined by a harmonic potential $V(\mathbf{r}) = \frac{1}{2} m^* \omega_o^2 r^2$ and subjected to an applied magnetic field in the symmetric gauge [$\mathbf{A}(\mathbf{r}) = \frac{1}{2} (\mathbf{B} \times \mathbf{r})$] in the spherical geometry [with $\mathbf{r} \equiv (r, \theta, \phi)$; see Fig. 1]. For such a typical Q0DES in the spherical quantum dot, the single-particle [of charge $-e$, with $e > 0$] Hamiltonian can be expressed as

$$H = \frac{1}{2m^*} \left[\mathbf{p} + \frac{e}{c} \mathbf{A} \right]^2 + \frac{1}{2} m^* \omega_o^2 r^2, \quad (1)$$

Where c , m^* , \mathbf{p} , \mathbf{A} , \mathbf{B} , and ω_o are, respectively, the speed of light in the vacuum, electron effective mass, momentum operator, vector potential, magnetic field, and the characteristic frequency of the harmonic oscillator. Obviously, we consider a one-component plasma inside the Q0DES and neglect the spin-orbit interactions and the Zeeman energy for the sake of simplicity. In the light of the Coulomb gauge [$\nabla \cdot \mathbf{A} = 0 \Rightarrow \mathbf{A} \cdot \mathbf{p} = \mathbf{p} \cdot \mathbf{A}$], the Hamiltonian in Eq. (1) can be written as

$$H = -\frac{\hbar^2}{2m^*} \nabla^2 + \frac{1}{2} \frac{eB}{m^* c} \hat{L}_z + \frac{1}{8} \frac{e^2}{m^* c^2} (\mathbf{B} \times \mathbf{r})^2 + \frac{1}{2} m^* \omega_o^2 r^2, \quad (2)$$

where the operator $\hat{L}_z = -i\hbar \frac{\partial}{\partial \phi}$ is the z -component of the angular momentum. Making use of the Laplacian operator ∇^2 (in the spherical coordinates), substituting $\Psi = R\Theta\Phi$ such that $\Psi(r, \theta, \phi) =$

$R(r)\Theta(\theta)\Phi(\phi)$, and transposing allows us to cast the Schrodinger equation $H\Psi = \epsilon\Psi - \epsilon$ being the eigenenergy – in the form

$$\begin{aligned} \frac{1}{R} \frac{d}{dr} \left(r^2 \frac{dR}{dr} \right) + \frac{2m^* r^2}{\hbar^2} \left[\epsilon - \frac{1}{2} \frac{eB}{m^* c} \hat{L}_z - \frac{1}{8} \frac{e^2}{m^* c^2} (\mathbf{B} \times \mathbf{r})^2 - \frac{1}{2} m^* \omega_o^2 r^2 \right] \\ + \frac{1}{\Theta \sin \theta} \frac{d}{d\theta} \left(\sin \theta \frac{d\Theta}{d\theta} \right) + \frac{1}{\Phi \sin^2 \theta} \frac{d^2 \Phi}{d\phi^2} = 0. \end{aligned} \quad (3)$$

What follows is the standard, lengthy but involved, mathematical procedure employing the method of separation of variables and searching the step-wise solutions beginning first with the last term in Eq. (3). The result is that the present system of QODES turns out to be characterized by the eigenfunction

$$\Psi(r, \theta, \phi) = R_{nl}(r) Y_l^m(\theta, \phi), \quad (4)$$

where the radial function

$$R_{nl}(r) = N_r e^{-X/2} X^{l/2} \Phi(-\alpha_{nl}; 1+s; X), \quad (5)$$

where $s = \frac{1}{2} + l$, $X = r^2/l_H^2$, and N_r is the normalization coefficient defined by

$$N_r^{-2} = \frac{1}{2} l_H^3 \int_0^{\bar{X}} dX e^{-X} X^S [\Phi(-\alpha_{nl}; 1+s; X)]^2, \quad (6)$$

where $\bar{X} = X|_{r=R}$, and $\Phi(-\alpha_{nl}; 1+s; X)$, $l_H = \sqrt{\hbar/(m^* \Omega_H)}$, $\Omega_H = \sqrt{\frac{\omega_c^2}{4} \sigma^2 + \omega_o^2}$, $\omega_c = eB/(m^* c)$, and R are, respectively, the confluent hypergeometric function (CHF) [45], the hybrid magnetic length, the hybrid characteristic frequency, the (electron) cyclotron frequency, and the dot radius. Figure 2 demonstrates that $\Phi(\dots)$ is unambiguously a well-behaved function over a wide range of X and α and that its period is seen to be decreasing with increasing X or α as the case may be. The spherical harmonics in Eq. (4) are defined as [46]

$$Y_l^m(\theta, \phi) = N_y P_l^m(\cos \theta) e^{im\phi}, \quad (7)$$

where $P_l^m(\cos \theta)$ is the associated Legendre function and N_y is the normalization coefficient defined by

$$N_y = \left[\frac{(2l+1)(l-m)!}{4\pi(l+m)!} \right]^{1/2}. \quad (8)$$

In Eqs (4) – (8) n , l , and m are, respectively, the principal, orbital, and magnetic quantum numbers. Remember that the spherical harmonics satisfy the orthonormality such as

$$\int d\Omega Y_l^{m*}(\theta, \phi) Y_{l'}^{m'}(\theta, \phi) = \delta_{ll'} \delta_{mm'} \quad (9)$$

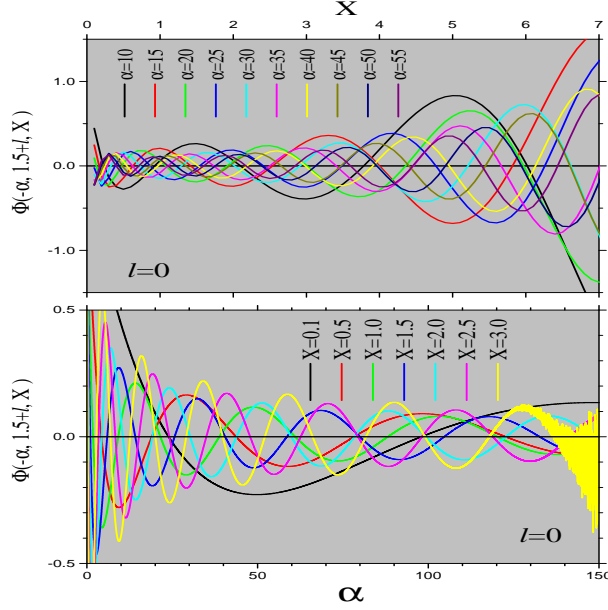


FIG. 2: (Color online) The plot of the confluent hypergeometric function (CHF) $\Phi(\alpha_{nl}; \frac{3}{2} + l; X)$ vs. X (the upper panel) and versus α (the lower panel), for $l = 0$. The purpose behind embedding this figure was/is to demonstrate that the CHF is a well-behaved function over a wide range of X and α_{nl} .

where the differential solid angle $d\Omega = \sin \theta d\theta d\phi$ and δ_{ij} is the well-known Kronecker delta function. The finiteness of the quantum dot requires that the eigenfunction $\Psi(\dots)$ satisfies the boundary condition $R_{nl}(r = R) = 0 \Rightarrow \Phi(-\alpha_{nl}; 1 + s; \bar{x}) = 0$. This determines the eigenenergy of the system defined by

$$\epsilon_{nlm} = 2 \hbar \Omega_H \left[\alpha_{nl} + \frac{1}{2} (1 + s) \right] + \frac{1}{2} m \hbar \omega_c \quad (10)$$

In the present form, the eigenenergy for the SQD is *formally* identical to that for the quantum dots laterally confined in the Q2DES [2]. Before we close this section, we think that it is important to pinpoint the appearance of a symbol σ in the definition of Ω_H above. Once we arrive at solving the radial part of the Schrodinger equation [see Eq. (3)], we realize that the third term in the square brackets in Eq. (3) contains an angular term, namely $\sin^2 \theta$. Of course, this is undesirable and therefore we want to get rid of it. The best strategy is to take the matrix elements of the whole (*radial*) equation between the states $|l, m\rangle$ and $|l', m'\rangle$. Doing this affects absolutely no other part of the radial equation and

converts this odd term into an expression defined by [47]

$$\begin{aligned}
\sigma^2 &= \langle l'm' | \sin^2 \theta | lm \rangle \\
&= \delta_{l'l} \delta_{m'm} - \left[\frac{(l+m+1)(l-m+1)}{(2l+1)(2l+3)} + \frac{(l+m)(l-m)}{(2l+1)(2l-1)} \right] \delta_{l'l} \delta_{m'm} \\
&\quad - \sqrt{\frac{(l+m)(l-m)(l+m-1)(l-m-1)}{(2l+1)(2l-1)^2(2l-3)}} \delta_{l',l-2} \delta_{m'm} \\
&\quad - \sqrt{\frac{(l+m+2)(l-m+2)(l+m+1)(l-m+1)}{(2l+5)(2l+3)^2(2l+1)}} \delta_{l',l+2} \delta_{m'm} \quad (11)
\end{aligned}$$

This indicates that the magnetic field can induce the coupling between the states l and $l \pm 2$. However, this coupling is irrelevant to the magneto-optical transitions to be discussed in what follows. Another important point is that the presence of the Kronecker delta functions [on both sides of the radial equation while taking the said matrix elements] finally disallows the existence of the third and fourth terms in the second equality of Eq. (11).

B. Density-density correlation function

The derivation of the density-density correlation function (DDCF) within the framework of Bohm-Pines' full-fledged RPA is the main part of the theoretical framework. As it was designed, the RPA in which the electrons respond only to the *total* (electric) potential accounts for the weak screened Coulomb interactions and hence is widely used for describing the nonlocal, dynamic, linear electronic response of the electron systems. To start with, we recall the single-particle density-density correlation function (DDCF), which is given by [2]

$$\chi^o(\mathbf{r}, \mathbf{r}'; \omega) = \sum_{ij} \Lambda_{ij} \Psi_i^*(\mathbf{r}) \Psi_j(\mathbf{r}) \Psi_j^*(\mathbf{r}') \Psi_i(\mathbf{r}'), \quad (12)$$

where

$$\Pi_{ij} = \frac{f(\epsilon_i) - f(\epsilon_j)}{\epsilon_i - \epsilon_j + \hbar\omega^+}, \quad (13)$$

where $f(\epsilon_j)$ is the standard Fermi-Dirac distribution function, $\Psi_j(\dots)$ is the single-particle eigenfunction [see Eq. (4)], and ϵ_j is the corresponding eigenenergy [see Eq. (10)]. The subindices $i, j \equiv n, l, m$ and $\omega^+ = \omega + i\gamma$, where small but nonzero γ refers to the adiabatic switching of the Coulombic interactions in the remote past [48]. Next, we make use of the Kubo's correlation function to write the induced particle density expressed as

$$n_{in}(\mathbf{r}, \omega) = \int d\mathbf{r} \chi(\mathbf{r}, \mathbf{r}'; \omega) V_{ex}(\mathbf{r}', \omega), \quad (14)$$

$$= \int d\mathbf{r} \chi^o(\mathbf{r}, \mathbf{r}'; \omega) V(\mathbf{r}', \omega), \quad (15)$$

where $V(\dots) = V_{ex}(\dots) + V_{in}(\dots)$ is the total potential, with suffix ex (in) referring to the external (induced) potential in the system. Here $\chi(\dots)[\chi^o(\dots)]$ is the interacting [single-particle] DDCF. Moreover, the induced potential is defined by

$$V_{in}(\mathbf{r}, \omega) = \int d\mathbf{r}' V_{ee}(\mathbf{r}, \mathbf{r}') n_{in}(\mathbf{r}', \omega), \quad (16)$$

where $V_{ee}(\dots)$ is the binary Coulombic interaction potential defined by

$$V_{ee}(\mathbf{r}, \mathbf{r}') = \frac{e^2}{\epsilon_o} \frac{1}{|\mathbf{r} - \mathbf{r}'|}, \quad (17)$$

where ϵ_o is the dielectric constant of the background the QODES is embedded in. Now, it is not quite difficult to derive, from Eqs. (14)-(17), the total [or interacting] DDCF that takes the form

$$\chi(\mathbf{r}, \mathbf{r}'; \omega) = \chi^o(\mathbf{r}, \mathbf{r}'; \omega) + \int d\mathbf{r}'' \int d\mathbf{r}''' \chi^o(\mathbf{r}, \mathbf{r}''; \omega) V_{ee}(\mathbf{r}'', \mathbf{r}''') \chi(\mathbf{r}''', \mathbf{r}'; \omega). \quad (18)$$

This is the famous Dyson equation in which the total DDCF $\chi(\dots)$ is, in general, a complex quantity. The Dyson equation can be cast in the form

$$\int d\mathbf{r}'' \epsilon(\mathbf{r}, \mathbf{r}''; \omega) \chi(\mathbf{r}'', \mathbf{r}'; \omega) = \chi^o(\mathbf{r}, \mathbf{r}'; \omega), \quad (19)$$

where the nonlocal, dynamic dielectric function $\epsilon(\mathbf{r}, \mathbf{r}'; \omega)$ is defined as follows.

$$\epsilon(\mathbf{r}, \mathbf{r}'; \omega) = \delta(\mathbf{r} - \mathbf{r}') - \int d\mathbf{r}'' \chi^o(\mathbf{r}, \mathbf{r}''; \omega) V_{ee}(\mathbf{r}'', \mathbf{r}'). \quad (20)$$

Multiplying on both sides of Eq. (19) by the inverse dielectric function $\epsilon^{-1}(\mathbf{r}'', \mathbf{r}; \omega)$, integrating over \mathbf{r} , and making use of the identity:

$$\int d\mathbf{r}'' \epsilon^{-1}(\mathbf{r}, \mathbf{r}'') \epsilon(\mathbf{r}'', \mathbf{r}') = \delta(\mathbf{r} - \mathbf{r}') \quad (21)$$

enables us to rewrite Eq. (19) in the form

$$\chi(\mathbf{r}, \mathbf{r}'; \omega) = \int d\mathbf{r}'' \chi^o(\mathbf{r}, \mathbf{r}''; \omega) \epsilon^{-1}(\mathbf{r}'', \mathbf{r}'; \omega). \quad (22)$$

The inverse dielectric function $\epsilon^{-1}(\mathbf{r}, \mathbf{r}'; \omega)$ was systematically derived for QNDES (with $N \equiv 2, 1, 0$) by Kushwaha and Garcia-Moliner [49] and is defined as follows.

$$\epsilon^{-1}(\mathbf{r}, \mathbf{r}'; \omega) = \delta(\mathbf{r} - \mathbf{r}') + \sum_{\mu\nu} L_{\mu}^*(\mathbf{r}) \Pi_{\mu} \Lambda_{\nu\mu} S_{\nu}(\mathbf{r}'), \quad (23)$$

where the symbols $L_{\mu}(\mathbf{r})$ and $S_{\mu}(\mathbf{r})$ representing, respectively, the long-range and the short-range parts of the response function are defined by

$$L_{\mu}(\mathbf{r}) = L_{ij}(\mathbf{r}) = \int d\mathbf{r}'' \Psi_i(\mathbf{r}'') V_{ee}(\mathbf{r}, \mathbf{r}'') \Psi_j^*(\mathbf{r}''), \quad (24)$$

$$S_{\mu}(\mathbf{r}) = S_{ij}(\mathbf{r}) = \Psi_j^*(\mathbf{r}) \Psi_i(\mathbf{r}), \quad (25)$$

and $\Lambda_{\mu\nu}$ is the inverse of $[\delta_{\mu\nu} - \Pi_\mu \beta_{\mu\nu}]$ such that

$$\sum_{\mu} \Lambda_{\gamma\mu} [\delta_{\mu\nu} - \Pi_\mu \beta_{\mu\nu}] = \delta_{\gamma\nu}, \quad (26)$$

where the symbol $\beta_{\mu\nu}$ stands for

$$\beta_{\mu\nu} = \int d\mathbf{r} L_{\mu}^*(\mathbf{r}) S_{\nu}(\mathbf{r}) \quad (27)$$

Notice that the subscript $\mu \equiv i, j$ is a composite index introduced just for the sake of the mathematical convenience [49]. Equation (22), with the aid of Eq. (23), can be rigorously expressed – [after suppressing the ω –dependence for the sake of brevity] – as

$$\chi(\mathbf{r}, \mathbf{r}'; \omega) = \sum_{ijkl} \left[\Pi_{ij} \delta_{ik} \delta_{jl} + \Pi_{ij} \sum_{mn} \Lambda_{klmn} \Pi_{mn} F_{mni j} \right] \Psi_i^*(\mathbf{r}) \Psi_j(\mathbf{r}) \Psi_l^*(\mathbf{r}') \Psi_k(\mathbf{r}'), \quad (28)$$

where the symbol F_{ijkl} stands for the matrix elements of Coulombic interactions and is expressed as

$$F_{mni j} = \int d\mathbf{r}'' \int d\mathbf{r}''' \Psi_m^*(\mathbf{r}'') \Psi_n(\mathbf{r}'') V_{ee}(\mathbf{r}'', \mathbf{r}''') \Psi_j^*(\mathbf{r}''') \Psi_i(\mathbf{r}''') \quad (29)$$

In order to investigate the magneto-optical absorption in the semiconducting SQDs, what we actually need to compute sagaciously is only the energy dependence of the *imaginary* part of $\chi(\dots)$, where

$$\begin{aligned} \chi(\omega) &= \int d\mathbf{r} \int d\mathbf{r}' \chi(\mathbf{r}, \mathbf{r}'; \omega) \\ &= \sum_{ijkl} \left[\Pi_{ij} \delta_{ik} \delta_{jl} + \Pi_{ij} \sum_{mn} \Lambda_{klmn} \Pi_{mn} F_{mni j} \right] \\ &\quad \times \int d\mathbf{r} \int d\mathbf{r}' \Psi_i^*(\mathbf{r}) \Psi_j(\mathbf{r}) \Psi_l^*(\mathbf{r}') \Psi_k(\mathbf{r}'). \end{aligned} \quad (30)$$

The only subtlety left out heretofore is the use of the Laplace expansion, which is, in fact, the expansion of the inverse distance between two points such as it occurs in the Coulomb potential. Let the points have position vectors \mathbf{r} and \mathbf{r}' , then the Laplace expansion is [50]

$$\frac{1}{|\mathbf{r} - \mathbf{r}'|} = \sum_{l=0}^{\infty} \sum_{m=-l}^l \frac{4\pi}{2l+1} \frac{r_{<}^l}{r_{>}^{l+1}} Y_l^{m*}(\theta, \phi) Y_l^m(\theta', \phi'), \quad (31)$$

where $r_{<}$ is the $\min(r, r')$ and $r_{>}$ is the $\max(r, r')$. Three simple steps – (i) write the inverse distance in the scalar form, (ii) deploy the generating function for the Legendre polynomial, and (iii) use the spherical harmonic addition theorem – allow the reader to derive the Laplace expansion in no time.

C. The optical transitions: Selection rules

In a completely confined system (as is the case here), the complex energy spectrum generally brings about complicated structures in the transport characteristics. The optical transitions, on the other

hand, follow selection rules and are simpler to analyze. Here we examine the interaction between an applied oscillating electric field E and the electric dipole moments of the electrons. The transition probability between the electronic states $|n, l, m\rangle$ and $|n', l', m'\rangle$ in the SQDs, according to Fermi's golden rule, is given by

$$M(n, l, m; n', l', m') = \frac{\pi}{2\hbar} \left| \langle n', l', m' | r \sin \theta e^{\pm i\phi} | n, l, m \rangle \right|^2, \quad (32)$$

whereas the transition amplitude is expressed as [47]

$$\begin{aligned} A(n, l, m; n', l', m') &= \langle n', l', m' | r \sin \theta e^{\pm i\phi} | n, l, m \rangle \\ &= \int d\mathbf{r} R_{n'l'}^*(r) Y_{l'}^{m'*}(\theta, \phi) r \sin \theta e^{\pm i\phi} R_{nl}(r) Y_l^m(\theta, \phi) \\ &= \int dr r^3 R_{n'l'}^*(r) R_{nl}(r) \int d\Omega Y_{l'}^{m'*}(\theta, \phi) \sin \theta e^{\pm i\phi} Y_l^m(\theta, \phi) \\ &= P(l, m) \int dr r^3 R_{n'l'}^*(r) R_{nl}(r), \end{aligned} \quad (33)$$

where the symbol $P(l, m)$ is defined as

$$P(l, m) = \begin{cases} + \left[\sqrt{\frac{(l+m+1)(l+m+2)}{(2l+1)(2l+3)}} \delta_{l', l+1} - \sqrt{\frac{(l-m)(l-m-1)}{(2l-1)(2l+1)}} \delta_{l', l-1} \right] \delta_{m', m+1}; & \text{for } + \text{ sign} \\ - \left[\sqrt{\frac{(l-m+1)(l-m+2)}{(2l+1)(2l+3)}} \delta_{l', l+1} - \sqrt{\frac{(l+m)(l+m-1)}{(2l-1)(2l+1)}} \delta_{l', l-1} \right] \delta_{m', m-1}; & \text{for } - \text{ sign} \end{cases} \quad (34)$$

Thus $P(l, m)$ already defines the selection rules for the orbital and the magnetic quantum numbers.

Equation (33), with the aid of Eq. (5), assumes the following form:

$$\begin{aligned} A(n, l, m; n', l', m') &= \frac{1}{2} P(l, m) N_r(n'l') N_r(nl) l_H^4 \\ &\quad \times \int dX e^{-X} X^{(S'+S+1)/2} \Phi(-\alpha_{n'l'}; 1+S'; X) \Phi(-\alpha_{nl}; 1+S; X). \end{aligned} \quad (35)$$

Since our main goal now is to determine the correlation between n' and n , it does not matter if we, for the moment, replace α_{nl} by n . Let us recall the identity relating the associated Laguerre polynomial $L_n^S(x)$ with the confluent hypergeometric function $\Phi(-n; 1+S; x)$:

$$L_n^S(x) = \binom{n+S}{n} \Phi(-n; 1+S; x). \quad (36)$$

The integral in Eq. (35), with the aid of Eq. (36), takes the form

$$I = \binom{n'+S'}{n'}^{-1} \binom{n+S}{n}^{-1} \int dX e^{-X} X^{(S'+S+1)/2} L_{n'}^{S'}(x) L_n^S(x) \quad (37)$$

$$= \begin{cases} \frac{n!(S+1)! S!}{(n+s)!} \left[\delta_{n', n} - \delta_{n', n-1} \right]; & s' = s + 1 \\ \frac{n'! S! (S-1)!}{(n'+s)!} \left[\delta_{n', n} - \delta_{n', n+1} \right]; & s' = s - 1. \end{cases} \quad (38)$$

Therefore the selection rules that follow from Eqs. (34) and (38) are: $\Delta n = 0, \pm 1$, $\Delta l = \pm 1$ and $\Delta m = \pm 1$. The corresponding transition energies are therefore specified by

$$\Delta\epsilon = 2 \left[\Delta\alpha \pm \frac{1}{2} \right] \hbar\Omega_H \pm \frac{1}{2} \hbar\omega_c \quad (39)$$

where $\Delta\alpha \equiv \Delta\alpha_{nl} = [\alpha_{1,1} - \alpha_{1,0}]$. As will be seen in the next section, the transition energy plotted against the magnetic field reveals some interesting features. For the zero confinement potential [i.e., $\hbar\omega_o = 0$], the transition is purely cyclotron resonance and the slope of the curve should define the electron effective mass m^* in a typical manner due, in particular, to the occurrence of the parameter σ and the term $\Delta\alpha$. For the zero magnetic field [i.e., $B = 0$], the transition will also differ from the case of $\Delta\epsilon = \hbar\omega_o$, again due to the presence of the term $\Delta\alpha$. Only in the case of laterally confined quantum dots do the corresponding cases become the first guess [2].

D. The Fermi energy

The Fermi energy is one of the most important concepts in the physics of solids as well as of quantum liquids such as the low-temperature liquid He (both normal and superfluid). Although, it is a single-particle aspect, it dictates largely the electron dynamics that is paramount to the understanding of electronic, optical, and transport phenomena in fermionic systems. Confusingly, the term Fermi energy is often used to refer to a different but closely related concept: the Fermi level – also called chemical potential. A few fundamental differences between the Fermi energy and the Fermi level are as follows: (i) the Fermi energy is only defined at absolute zero, while the Fermi level is defined for any temperature, (ii) the Fermi energy is an energy difference, whereas the Fermi level is a total energy level (including the kinetic and potential energies), and (iii) the Fermi energy can only be defined for non-interacting fermions, whereas the Fermi level remains well defined even in complex interacting systems.

Since each quantum level takes two electrons with opposite spin, the Fermi energy ϵ_F of a system of N non-interacting electrons at absolute zero is actually the energy of the $(\frac{1}{2}N)$ th level. In the case of a quantum dot containing N electrons – with complete confinement – the Fermi energy can be computed self-consistently through the following expression:

$$N = 2 \sum_{nlm} \theta(\epsilon_F - \epsilon_{nlm}), \quad (40)$$

where the ϵ_{nlm} is as defined in Eq. (10). In a completely confined system of quantum dots, the single-particle excitation spectrum [see Sec. III] turns out to be quite complex and therefore the Fermi energy cannot be expected to be a smooth function of the magnetic field. The most striking characteristic of the semiconducting SQDs is the size-dependence of the Fermi level brought about by the variations

in the density of electronic states due, in fact, to the framed bounds of the nanocrystal. This can be understood by recalling the Heisenberg's uncertainty principle in relation between position and momentum in free and confined particles. For a free particle, or a particle in the periodic potential of an extended crystal, the momentum can be precisely defined, but the position cannot. For a confined particle, while the uncertainty in the position decreases, the momentum is no longer well-defined. The result is that the close by transitions occurring at slightly different energies in an extended crystal will be squeezed by the quantum confinement into a single, energetic transition in a quantum dot.

III. ILLUSTRATIVE EXAMPLES

In order to discuss the illustrative numerical examples, it is indispensable to specify the material the quantum dots are made of and the parameters used in the computation. We consider colloidally prepared GaAs spherical quantum dots, which implies that the background dielectric constant $\epsilon_o = 12.8$ and the effective mass of the electron $m^* = 0.067 m_o$, where m_o is the mass of the bare electron. The other parameters involved in the computation are: the radius of the quantum dot (R), the confinement potential $\hbar\omega_o$, and the magnetic field B ; which will be stated while discussing the specific results for the respective cases. It is also imperative to limit the number of electrons – or, in other words, to specify the quantum numbers n , l , and m – while computing the optical (or magneto-optical) absorption in the system [see, e.g., Eqs. (28) or (30)]. This is equivalent to truncating the $\infty \times \infty$ matrix in the band structure computation in solid state physics by limiting, for example, the number of plane waves. Until and unless stated otherwise, we have specified the quantum numbers such that the quantum dot contains in total *twenty four* electrons (including spin). It is noteworthy that we also assume the compliance of the lowest subband approximation due to the harmonic confinement potential, which makes sense for the quantum dots with small charge densities at low temperatures where most of the experiments are performed on the low-dimensional systems. For the sake of comparison, we also discuss briefly the results for the case of zero magnetic field.

A. The zero magnetic field:

Figure 3 illustrates the single-particle excitation spectrum for the harmonically confined SQDs in the absence of an applied magnetic field. The plots are rendered in terms of the dimensionless variables: ϵ_{nl}/ϵ_r and $\zeta = R^2/l_o^2$. Here $\epsilon_r = 2\hbar^2/(m^* R^2)$, and $l_o = \sqrt{\hbar/(m^*\omega_o)}$ is the characteristic length due to the harmonic confinement. Most of the modes start from zero with close to zero group velocity, which becomes gradually positive as the excitation energy increases with increasing ζ . At large values of ζ , there is a set of j (with $j \geq 2$) branches – belonging to different quantum numbers n and l – that are

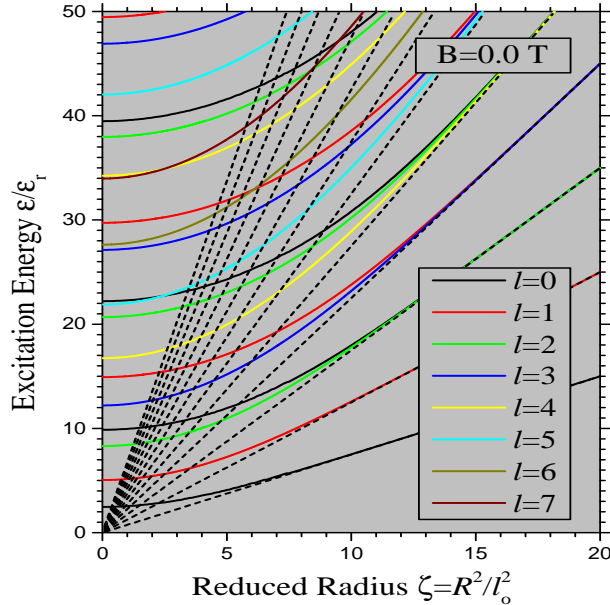


FIG. 3: (Color online) The single-particle excitation spectrum for the GaAs SQDs in the absence of an applied magnetic field, i.e. $B = 0$, for several values of the orbital quantum number l . The electric fan plotted as dashed lines is a zero magnetic-field analogue of the magnetic (or Landau) fan. The symbols are as defined in the text.

seen to merge together. We find that one such set can be generated by $\sum_{k=1}^n [n - (k - 1), 2(k - 1)]$ and the other by $\sum_{k=1}^n [n - (k - 1), (2k - 1)]$, with $n \geq 2$. Thus, the coalesced branches in terms of (n, l) are: $(2, 0) + (1, 2)$; $(3, 0) + (2, 2) + (1, 4)$; $(2, 1) + (1, 3)$; and $(3, 1) + (2, 3) + (1, 5)$. The dashed lines represent the *electric* fan due to the confinement given by $\epsilon/\epsilon_r = \zeta [l + \frac{3}{2}]$ – analogous to the *magnetic* (or Landau) fan for the non-zero magnetic field. For very large confinement potential, we obtain the ideal 3D limit defined by $\epsilon_{nl} = \frac{3}{2} \hbar \omega_o$. We believe that the transport measurements on SQDs should be capable to map the excitation energy levels shown in Fig. 3

Figure 4 shows the optical absorption, i.e., $\text{Im}\chi(\omega)$ [see Eq. (30)], versus the excitation energy for a given confinement potential $\hbar\omega_o = 5$ meV and for several values of the dot radius. We consider the quantum dots with radii lying in the range defined by $25 \leq R$ (nm) ≤ 45 . This size range is known to be quite easily attainable in the colloiddally prepared SQDs. Note that we have scaled down the vertical axis with no loss of generality. What we observe is that as the size of the quantum dot is reduced, the absorption peak undergoes a blue shift (in energy). In other words, diminishing the dot-size pushes the (*localized*) plasmon excitations to shift to higher energy, thereby restricting the oscillator strength to be concentrated into just a few transitions. The quantum confinement brings about these physical occurrences due to the changes in the electronic density of states. This implies that tailoring the size of the quantum dots leads us to tune the electronic excitations at will.

Figure 5 depicts the optical absorption as a function of the excitation energy for a given dot radius

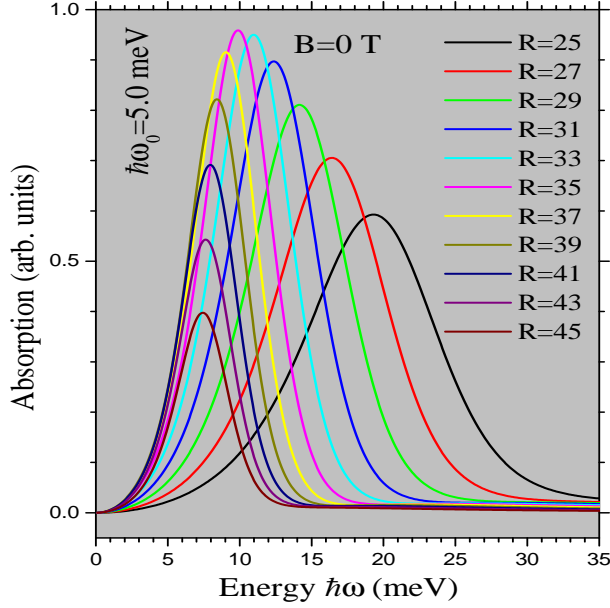


FIG. 4: (Color online) The optical absorption vs. the excitation energy for the GaAs SQDs in the absence of an applied magnetic field, for several values of the dot radius R . The confinement potential $\hbar\omega_o = 5$ meV.

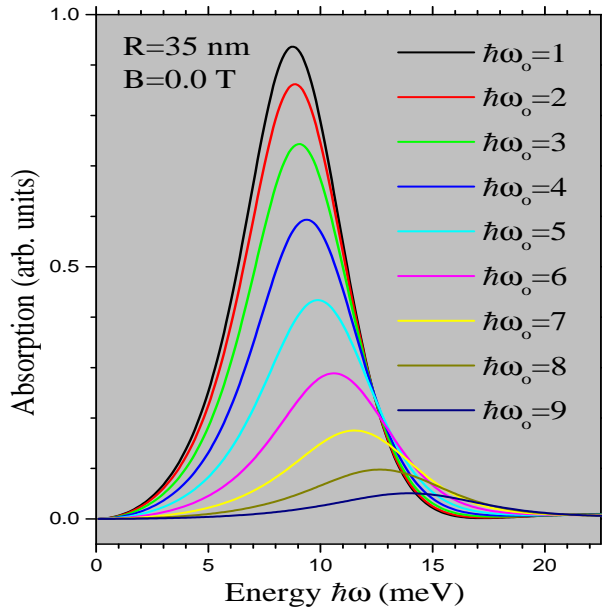


FIG. 5: (Color online) The optical absorption vs. the excitation energy for the GaAs SQDs in the absence of an applied magnetic field, for several values of the confinement potential $\hbar\omega_o$. The dot radius $R = 35$ nm.

$R = 35$ nm and for several values of the confinement potential ($1 \leq \hbar\omega_o$ (meV) ≤ 9). We observe that the absorption peak height (width) reduces (broadens) with increasing confinement potential. It is important to notice that the peak position observes a blue shift as the confinement potential grows. To be specific, we notice that if the confinement grows by a factor of nine, the peak position experiences a blue-shift of 60%. This is understandable: the stronger the confinement potential, the smaller the space

available to the electrons (or greater the degree of localization). This implies virtually the reduction in the dot size and hence the blue shift of the absorption peaks.

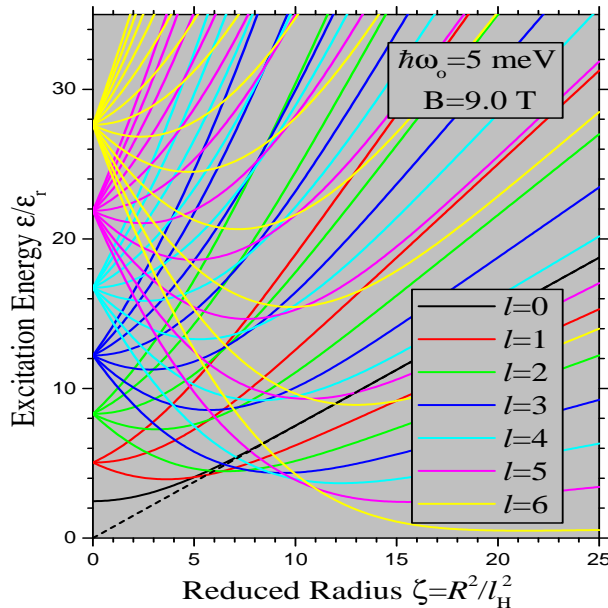


FIG. 6: (Color online) The single-particle excitation spectrum for the GaAs SQUIDs in the presence of an applied magnetic field (B), for several values of the orbital quantum number $l \leq 6$. The dashed line represents the lowest branch of the magnetic (or Landau) fan – when $\alpha_{nl} \rightarrow 0$ for very large R or B . The magnetic field $B = 9$ T and the confinement potential $\hbar\omega_o = 5$ meV.

B. The non-zero magnetic field:

Figure 6 represents the single-particle excitation spectrum for the spherical quantum dot in the presence of a confinement potential ($\hbar\omega_o = 5$ meV) and an applied magnetic field ($B = 9$ T) for the orbital quantum number $l \leq 6$. The plots are rendered in terms of the dimensionless energy $\epsilon_{nlm}/\epsilon_r$ and the dot radius $\zeta = R^2/l_H^2$. Here $l_H = \sqrt{\hbar/(m^*\Omega_H)}$ is the hybrid magnetic length [see Sec. II.A] and ϵ_r is just as defined above. First and foremost, we observe that, unlike the laterally confined 2D quantum dots [2], the electronic levels at the origin [i.e., at $\zeta = 0$] are not equispaced. This is clearly attributed to the geometrical difference more than anything else. This remark is also valid in relation with Fig. 3. The $(2l + 1)$ -degeneracy at the origin justifies the intuition. All the modes with $m \geq 0$ are seen to start and propagate throughout with a positive group velocity, whereas those with $m < 0$ start with a negative group velocity, attain a minimum as ζ increases, and finally propagate with the positive group velocity. It is noticeable that the larger the $|m|$, the greater the value of ζ where the latter type of modes observe the minimum. The dashed line starting from zero and finally merging with $(l = 0 = m)$ mode – the ground state – is the lowest branch of the magnetic [or Landau] fan. We

did not plot the whole magnetic fan in order not to make a mess inside the figure. At large values of magnetic field – keeping the dot radius and the confinement potential fixed – ζ becomes large, the role of α_{nl} diminishes and the magnetic fan is born. In case the confinement energy predominates over the cyclotron energy (i.e., $\hbar\omega_o \gg \hbar\omega_c$), Fig. 3 is reinstated.

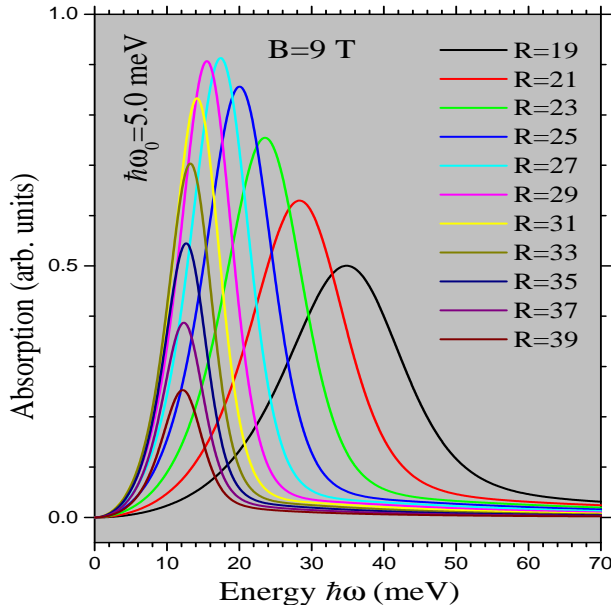


FIG. 7: (Color online) The magneto-optical absorption vs. the excitation energy for the GaAs SQRDs in the presence of an applied magnetic field (B), for several values of the dot radius R . The magnetic field $B = 9$ T and the confinement potential $\hbar\omega_o = 5$ meV.

Figure 7 portrays the magneto-optical absorption as a function of the excitation energy for a given value of the confinement potential ($\hbar\omega_o = 5$ meV) and the magnetic field ($B = 9.0$ T), for several values of the dot radius ($19 \leq R$ (nm) ≤ 39). It is observed that the absorption peak experiences a blue shift as the dot radius is decreased. A similar observation was made in the case of a zero magnetic field [see, e.g., Fig. 4]. Comparing Fig. 7 with Fig. 4 leads us to notice that the magnetic field enhances the blue shift for a given dot size. In other words, the magnetic field prompts the quantum dot to absorb photons with higher energies. For example, for $R = 35$ nm [$R = 39$ nm] the energy peak has blue-shifted by 31% [46%]. This also indicates that the larger the dot size, the greater the effect of the magnetic field. This seems to make sense. In a very constricted dot, the charge carriers do not have sufficient room to respond to and hence to feel the effect of an applied magnetic field. It has also been noticed that the FWHM of the absorption peak increases with decreasing dot size.

Figure 8 sketches the magneto-optical absorption versus the excitation energy for a given value of the dot size ($R = 35$ nm) and the magnetic field ($B = 15$ T), for several values of the confinement potential ($1 \leq \hbar\omega_o$ (meV) ≤ 9). One observation – common to Fig. 7 – is that the absorption peak is

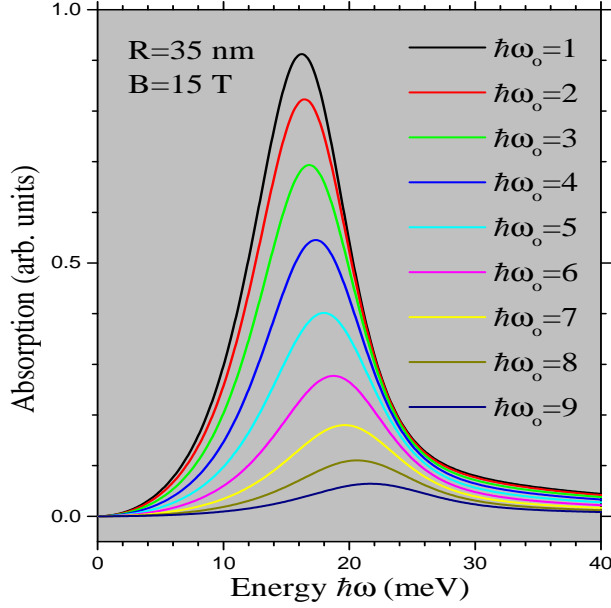


FIG. 8: (Color online) The magneto-optical absorption vs. the excitation energy for the GaAs SQDs in the presence of an applied magnetic field (B), for several values of the confinement potential $\hbar\omega_o$. The magnetic field $B = 15$ T and the dot radius $R = 35$ nm.

blue-shifted as the confinement potential increases. A similar effect was observed in relation with Fig. 5 for the zero magnetic field. To be specific, we notice that for $\hbar\omega_o = 1, 5, 9$ meV the absorption peak has blue-shifted, respectively, by 84%, 82%, and 55%. This also shows that the stronger the confinement, the weaker the blue-shift experienced by the absorption peaks. Again, the FWHM of the absorption peak increases with increasing confinement. This also reflects the tendency of the oscillator strength focused into a fewer transitions for the stronger confinement.

Figure 9 renders the magneto-optical absorption against the excitation energy for a given value of the dot size ($R = 25$ nm) and the confinement potential ($\hbar\omega_o = 5$ meV), for several values of the applied magnetic field ($1 \leq B$ (T) ≤ 33). A few first-hand observations are: the peak height decreases, FWHM increases, and the blue-shift is enhanced with increasing intensity of the applied magnetic field. To be a little bit more specific, we observe that increasing the magnetic field from $B = 1$ T to $B = 25$ T results in the absorption peak's blue-shift by 52% for the present set of parameters. This defines the role of an applied magnetic field in the optical absorption of spherical quantum dots. That is the stronger the magnetic field, the greater the capacity of the quantum dots to absorb the photons of higher energy. The other remarks regarding the oscillator strength about Fig. 8 are still valid. By and large, the size effects predominate over those due to confinement and magnetic field.

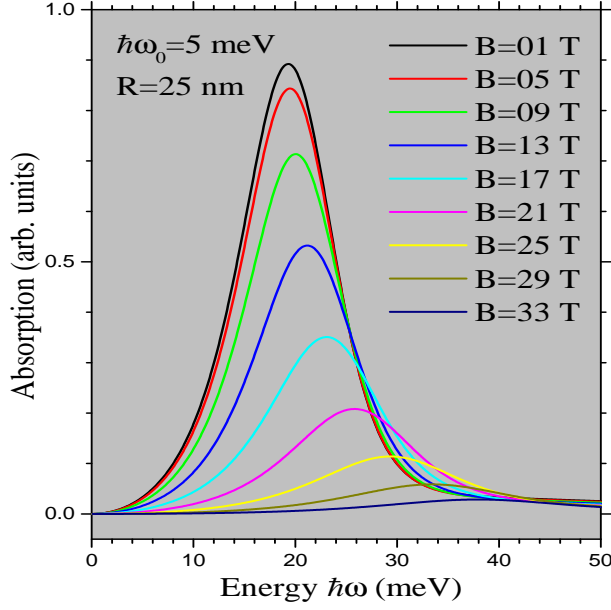


FIG. 9: (Color online) The magneto-optical absorption vs. the excitation energy for the GaAs SQUIDs in the presence of an applied magnetic field (B), for several values of the magnetic field B . The dot radius $R = 25$ nm and the confinement potential $\hbar\omega_o = 5$ meV.

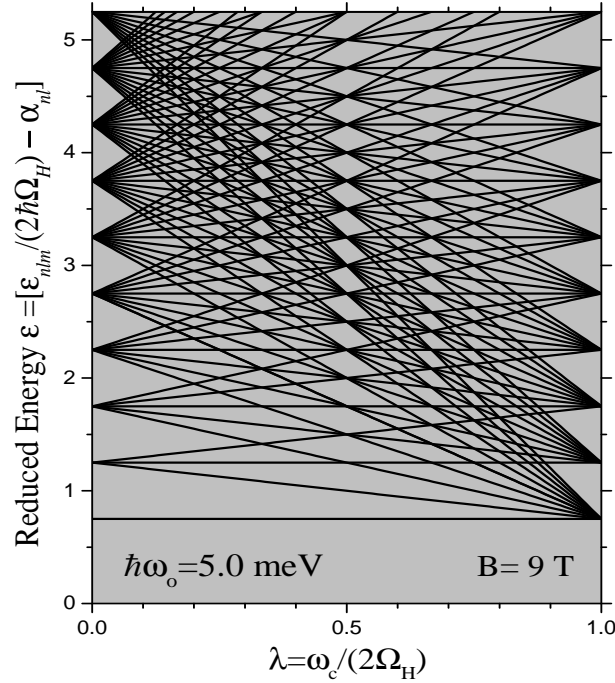


FIG. 10: (Color online) The zigzag representation of the single-particle excitation spectrum for the GaAs SQUIDs for the confinement potential $\hbar\omega_o = 5$ meV and the magnetic field $B = 9$ T [see the text for the expression of ϵ]. Notice that following the state ($l = 1$), crossings with states of ($l < 0$) occur at $\lambda = (l - 1)/(l + 1)$.

C. Other field-effects in SQDs

Figure 10 draws the zigzag type of single-particle excitation spectrum for SQDs in the presence of an applied magnetic field ($B = 9$ T) and the confinement potential ($\hbar\omega_o = 5$ meV). Specifically, we plot the dimensionless energy $\epsilon [= \epsilon_{nlm}/(2\hbar\Omega_H) - \alpha_{nl}] = \frac{1}{2}(\frac{3}{2} + l) + \frac{1}{2}m\lambda$ versus the dimensionless parameter $\lambda = \omega_c/(2\Omega_H)$ [see Eq. (10)]. The interest in such eigenenergies as plotted in this figure lies in the fact that they allow us to debate the gradual transitions from pure spatial quantization [$\omega_o \neq 0$, $\omega_c = 0$, $\lambda = 0$] to pure magnetic quantization [$\omega_o = 0$, $\omega_c \neq 0$, $\lambda = 1$]. In this representation each state ψ_{nlm} corresponds to one straight line with slope given by $\frac{1}{2}m$. For $m \leq 0$, the quantum number l dictates the crisscrossing with the vertical axis $\lambda = 1$. At $\lambda = 0$, the $(2l+1)$ -degeneracy is given by the ϵ , whereas at $\lambda = 1$, we acquire the familiar macroscopic degeneracy of magnetic (or Landau) levels. Note that we have limited to states with orbital quantum number $l \leq 9$, otherwise there would be innumerable number of lines of increasing slope emerging from each of the levels at $\lambda = 1$. Obviously, only ($l = 0 = m$) states are independent of λ and constitute the straight lines with zero slope. Following the state ($l = 1$), crossings with states of ($l < 0$) occur at $\lambda = (l - 1)/(l + 1)$.

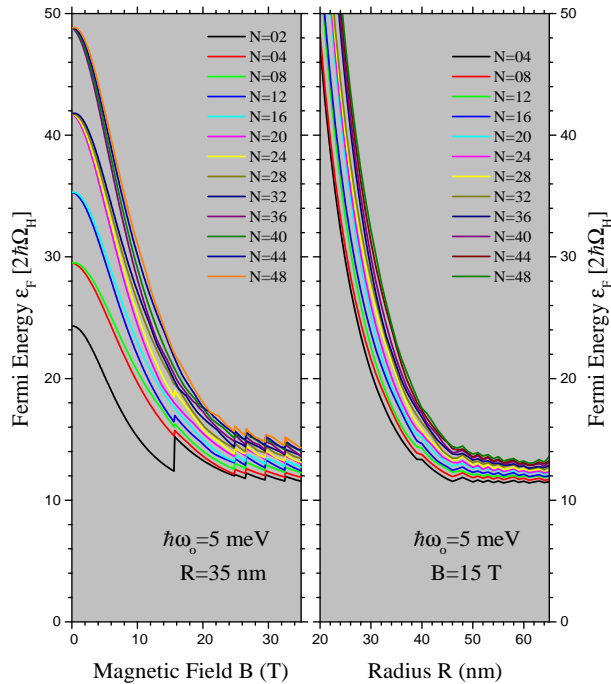


FIG. 11: (Color online) The Fermi energy of the N -particle GaAs spherical quantum dot as a function of the magnetic field (B) [the left panel] and the dot radius (R) [the right panel], for the confinement potential $\hbar\omega_o = 5$ meV. The dot radius $R = 35$ nm [in the left panel] and the magnetic field $B = 15$ T [in the right panel].

Figure 11 presents the dot-size and magnetic-field dependence of the Fermi energy, self-consistently computed through Eq. (40), for several numbers of the electrons comprising the quantum dot. The

left (right) panel shows the magnetic-field (dot-size) dependence of the Fermi energy for a given value of the confinement potential ($\hbar\omega_o = 5$ meV) for $4 \leq N \leq 48$. We fix the dot-size (magnetic field) to be $R = 35$ nm ($B = 15$ T) in the left (right) panel. It is observed that the Fermi energy gradually decreases with increasing magnetic field or the dot-size. At large magnetic fields, the Fermi energy is seen to be making saw-tooth-like oscillations with increasing B . The similar, but less pronounced, behavior is noticed at larger dot-size in the right panel. However, the larger the number of electrons, the greater the Fermi energy for all values of magnetic field and dot-size, just as intuitively expected. It is not difficult to demonstrate analytically that the Fermi energy becomes asymptotic to the x-axis – and hence attains a zero slope – at large values of B and R . To this end, while the B -dependence in Eq. (10) is obvious, the R -dependence is not. To be laconic, α_{nl} , which is determined by enforcing the proper boundary condition [see Sec. II.A], diminishes at large B as well as at large R .

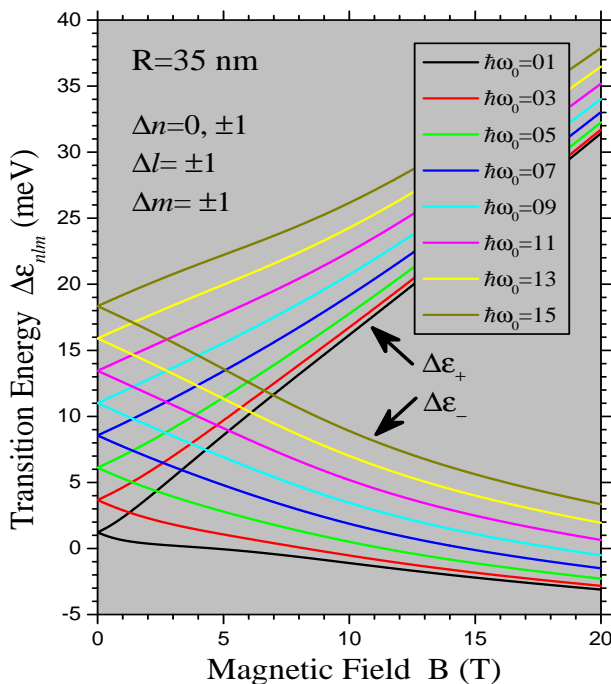


FIG. 12: (Color online) Allowed magneto-optical transitions as a function of the magnetic field (B), for several values of the confinement potential $\hbar\omega_o$. The dot radius is defined as $R = 35$ nm. The selection rules are listed in the picture. The upper (lower) transition is designated as $\Delta\epsilon_+$ ($\Delta\epsilon_-$).

Figure 12 describes the magneto-optical transitions in the spherical quantum dots as a function of magnetic field for a given value of the dot size ($R = 35$ nm), for several values of the confinement potential ($01 \leq \hbar\omega_o$ (meV) ≤ 15). Figure 12 is actually based on the computation of the exact analytical expression for the transition energy in Eq. (39). The selection rules derived in Sec. II.C are as listed inside the picture. Some simple mathematical manipulations of Eq. (39) reveal that, unlike the laterally confined quantum dots [2, 51], both transitions – upper [$\Delta\epsilon_+$] and lower [$\Delta\epsilon_-$] – will always survive

whether or not $\hbar\omega_o = 0$. Similarly, at $B = 0$, we are still left with two, albeit relatively weaker, transitions given by $\Delta\epsilon_{\pm} = 2[\Delta\alpha \pm \frac{1}{2}] \hbar\omega_o$. Even when $B \rightarrow \infty$ – i.e., $\omega_c \gg \omega_o$ – we cannot avoid either of the two transitions. In other words, the SQDs do not allow the intra-Landau level transitions. The presence of the parameters σ and α_{nl} disallow the edges of the wedges to be exactly characterized by the confinement potential ($\hbar\omega_o$) at $B = 0$. These findings should encourage magneto-optical experiments aimed at verifying such details in SQDs.

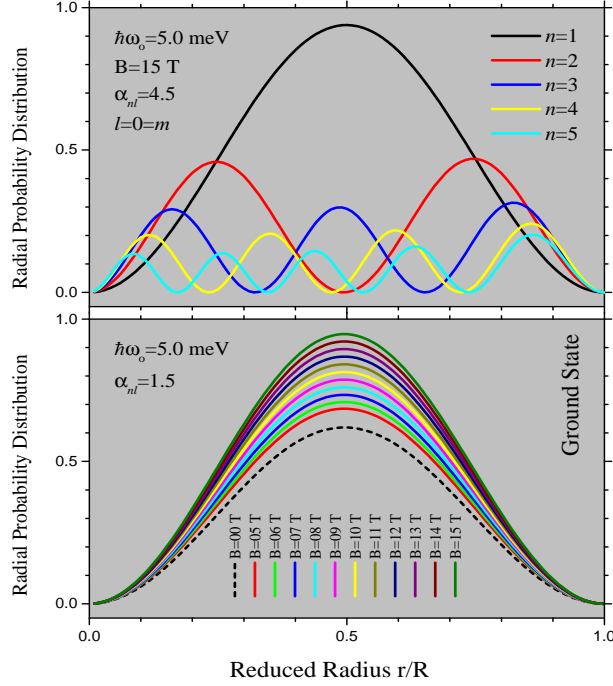


FIG. 13: (Color online) The radial probability distribution $Q_{nl}(r)$ in the ground state for the GaAs SQDs against the reduced (radial) coordinate r/R . The confinement potential $\hbar\omega_o = 5$ meV). The magnetic field $B = 15$ T in the upper panel for the ground state, for several values of the principal quantum number n , which distinguishes the s orbitals characterized by $l = 0$. The number of nodes equals $(n - 1)$. The lower panel shows $Q_{nl}(r)$ in the ground state ($n = 1, l = 0, m = 0$) for several values of magnetic field B .

Figure 13 shows the radial probability distribution in the ground state for the GaAs SQDs against the reduced radial coordinate r/R for a given confinement potential ($\hbar\omega_o = 5$ meV). The radial probability distribution $Q_{nl}(r)$ defined as $Q_{nl}(r) = \int_0^\pi d\theta \sin \theta \int_0^{2\pi} d\phi r^2 |\Psi(r, \theta, \phi)|^2$ expresses the probability of finding an electron as a function of r at a given instant. Before we proceed further, it is worthwhile to remember that the (involved) associated Legendre function $P_l^m(x) = 1$ for the quantum numbers $l = 0 = m$, irrespective of its argument (x). The upper panel plots the ground states ($l = 0, m = 0$) along with $n = 1, n = 2, n = 3, n = 4$, and $n = 5$, for the magnetic field $B = 15$ T. In the language of *spectroscopy*, the principal quantum n distinguishes the s orbitals – characterized by $l = 0$. The number of nodes – i.e., the values of r where the $Q_{nl}(r)$ is zero – equals $(n - 1)$.

The lower panel of Fig. 13 exhibits the probability distribution in the ground state for several values of the magnetic field in the range $0 \leq B \text{ (T)} \leq 15$. Note that $Q_{nl}(r)$ is zero at $r = 0$ because the volume of space available $r^2 dr = 0$. As r increases, the dot size increases and so does $Q_{nl}(r)$. However, the probability density $|\Psi(r, \theta, \phi)|^2$ decreases with increasing r , which implies that the $Q_{nl}(r)$ -path must have observed a maximum, where the probability of locating the electron is eminent. The influence of an applied magnetic field on the variation of $Q_{nl}(r)$ is interesting to notice. We find that the magnetic field tends to further add to the confinement and hence maximize the probability distribution with increasing B . The crux of the matter is that the magnetic field does not shift the peak position of the radial distribution, which lies at $r/R \simeq 0.495$ for the whole range of B , including $B = 0$.

IV. CONCLUDING REMARKS

In summary, we thoroughly investigated the magneto-optical absorption in the colloiddally prepared spherical GaAs quantum dots in the presence of a confining harmonic potential and an applied magnetic field in the symmetric gauge. The theoretical formulation is constituted within the framework of Bohm-Pines' full-fledged RPA enabling us to derive the Dyson equation for the total (or interacting) density-density correlation function. For this purpose, we employ the exact single-particle eigenfunctions and eigenenergies obtained in Sec. II.A and the strategy of determining the non-local, dynamic *inverse* dielectric function from Ref. 49. This served us to analyze the Fermi's golden rule in order to derive the selection rules for the magneto-optical transitions and extract the right expression for the radial probability distribution for the SQDs. Studying the size-dependence of the Fermi energy for the SQDs was a part of this theoretical goal. All illustrative examples discussed here are thus the outcomes of the computation based on the exact analytical results.

The magneto-optical absorption peak is blue-shifted with decreasing dot-size, increasing confinement, and with increasing magnetic field. The larger dot-size and stronger magnetic field can enable us to debate the gradual transitions from pure spatial to pure magnetic quantization. At lower dot-size and weaker magnetic field, the Fermi energy decreases with increasing size and field. For large dot-size and strong magnetic fields, the Fermi energy makes saw-tooth-like oscillations and finally becomes insensitive to both of them. It is not difficult to justify this behavior analytically. The SQDs always allow both (upper and lower) transitions to survive even in the extreme cases of vanishing confinement or magnetic field. While the magnetic field tends to maximize the probability of finding the electron, it does not shift the peak position of the radial distribution. These findings should motivate the magneto-optical experiments on SQDs aimed at verifying such details as listed here.

What is so special about the spherical geometry (SG)? It is a historical fact that the SG has played

a model role for testing various classical and quantal hypotheses in the past. One of the latest instances is the use of the SG for studying the fractional quantum Hall effect (FQHE) [52]. Here a 2D sheet of electrons is wrapped up on a spherical surface exposed to a radial magnetic field generated by a Dirac magnetic monopole placed at the center of the sphere. The motivations behind the SG are two-fold [53]: First, it is free from edges, which makes it potentially fit for studying the bulk properties. Second, Landau levels (LLs) have a finite degeneracy (for a finite magnetic field), which helps discern incompressible states for finite systems. The SG has been pivotal in constructing the theory of FQHE and in furnishing proofs for numerous related features.

Despite the in-depth research pursuits of electronic, optical, and transport phenomena in quantum dots in the past, our practical knowledge required to harness the full potential of these man-made atoms still seems to be in its infancy. It has been instructive to inquire into the addition spectra using the concept of *Coulomb blockade* that helps provide control over the number of electrons by adjusting the energy required. The exchange interaction plays a role and the energy needed to add a second electron in the presence of an existing one also depends upon their relative spin. The long life-time of the (restricted) electron-electron interactions commonly gives rise to *decoherence*, implying that the dots can offer a potential system for exploring technologies based upon the quantum coherence. As an example, it is likely to create and control superimposed or even *entangled* states using the highly coherent lasers. External control over the full quantum eigenfunction in a semiconducting SQD may even lead to exciting applications such as those involving quantum computing.

Acknowledgments

The author would like to express his sincere thanks to Loren Pfeiffer, Daniel Gammon, and Aron Pinczuk for the very useful communication regarding the fabrication of the spherical quantum dots. He would also like to thank Peter Nordlander, Naomi Halas, and Thomas Killian for all the support and encouragement. He appreciates Kevin Singh for the unconditional help with the software.

-
- [1] The origin of the lower dimensional systems dates back to 1957 when Schrieffer [J.R. Schrieffer, in: R.H. Kingston (Ed.), *Semiconductor Surface Physics* (University of Pennsylvania Press, Philadelphia, PA, 1957) p. 55] anticipated the quantization of energy levels in inversion layers. But the two-dimensional (2D) nature of electron gas – when only the lowest electric subband is occupied – was first confirmed experimentally by Fowler et al. [A.B. Fowler, F.F. Fang, W.E. Howard, P.J. Stiles, *Phys. Rev. Lett.* **16**, 901 (1966)] in 1966.
- [2] For an extensive review of electronic, optical, and transport phenomena in the systems of reduced dimensions such as quantum wells, quantum wires, quantum dots, and (electrically/magnetically) modulated quantum systems, see M.S. Kushwaha, *Surf. Sci. Rep.* **41**, 1 (2001).
- [3] L. Esaki and R. Tsu, *IBM J. Res. Dev.* **14**, 61 (1970).
- [4] H. Sakaki, *Jpn. J. Appl. Phys.* **19**, L735 (1980).
- [5] Y. Arakawa and H. Sakaki, *Appl. Phys. Lett.* **40**, 939 (1982).
- [6] A.L. Efros and A.L. Efros, *Sov. Phys.: Semiconductors* **16**, 772 (1982).
- [7] L.E. Brus, *J. Chem. Phys.* **80**, 4403 (1984).
- [8] L. Banyai and S.W. Koch, *Phys. Rev. Lett.* **57**, 2722 (1986).
- [9] M.L. Steigerwald and L.E. Brus, *Annu. Rev. Mater. Sci.* **19**, 471 (1989).
- [10] Y. Wang and N. Herron, *J. Phys. Chem.* **95**, 525 (1991).
- [11] L.M. Ramaniah and S.V. Nair, *Phys. Rev. B* **47**, 7132 (1993).
- [12] A.P. Alivisatos, *Science* **271**, 933 (1996).
- [13] Zh. Xiao, *J. Appl. Phys.* **86**, 4509 (1999).
- [14] Daniel Gammon, *Nature* **405**, 899 (2000).
- [15] M.Bayer, O. Stern, P. Hawrylak, S. Fafard, and A. Forshel, *Nature* **405**, 923 (2000).
- [16] R.J. Warburton, C. Schafflein, D. Haft, F. Bickel, A. Lorke, K. Karrai, J.M. Garcia, W. Schoenfeld, and P.M. Petroff, *Nature* **405**, 926 (2000).
- [17] J. Kainz, S.A. Mikhailov, A. Wensauer, and U. Rossler, *Phys. Rev. B* **65**, 115305 (2002).
- [18] R.D. Schaller and V.I. Klimov, *Phys. Rev. Lett.* **92**, 186601 (2004).
- [19] M.Tadic and F.M. Peeters, *Phys. Rev. B* **71**, 1125342 (2005).
- [20] C. Simserides, A. Zora, and G. Triberis, *Phys. Rev. B* **73**, 155313 (2006).
- [21] J.Z. Zhang and I. Galbraith, *Phys. Rev. B* **77**, 205319 (2008).
- [22] J.W. Luo, A. Franceschetti, and A. Zunger, *Phys. Rev. B* **78**, 035306 (2008).
- [23] T. Schwarzl, E. Kaufmann, G. Springholz, K. Koike, T. Hotei, M. Yano, and W. Heiss, *Phys. Rev. B* **78**, 165320 (2008).
- [24] Th. Puangmali, M. Califano, and P. Harrison, *Phys. Rev. B* **78**, 245104 (2008).
- [25] M.B. Harouni, R. Roknizadeh, and M.H. Naderi, *Phys. Rev. B* **79**, 165304 (2009).
- [26] J.L. Movilla, A. Ballester, and J. Planelles, *Phys. Rev. B* **79**, 195319 (2009).
- [27] S.V. Goupalov, *Phys. Rev. B* **79**, 233305 (2009).
- [28] C.L. Weng and Y.C. Tsai, *Phys. Rev. B* **79**, 245327 (2009).

- [29] P. Horodyska, P. Nemeč, D. Sprinzl, P. Maly, V.N. Gladilin, and J.T. Devreese, Phys. Rev. B **81**, 045301 (2010).
- [30] M. Genkin and E. Lindroth, Phys. Rev. B **81**, 125315 (2010).
- [31] L. Silvestri and V.M. Agranovich, Phys. Rev. B **81**, 205302 (2010).
- [32] Th. G. Pedersen, Phys. Rev. B **81**, 233406 (2010).
- [33] C.Y. Lin and Y.K. Ho, Phys. Rev. B **84**, 023407 (2011).
- [34] S. Wu and L. Wan, J. Appl. Phys. **111**, 063711 (2012).
- [35] H.P. Paudel and M.N. Leuenberger, Phys. Rev. B **88**, 085316 (2013).
- [36] W. Kohn, Phys. Rev. **123**, 1242 (1961).
- [37] F. M. Peeters, Phys. Rev. B **42**, 1486 (1990); P.A. Maksym and T. Chakraborty, Phys. Rev. Lett. **65**, 108 (1990).
- [38] M.S. Kushwaha, Phys. Rev. B **74**, 045304 (2006).
- [39] M.S. Kushwaha, Phys. Rev. B **76**, 245315 (2007).
- [40] M.S. Kushwaha, J. Appl. Phys. **104**, 083714 (2008).
- [41] D. Pines, *The Many-Body Problem* (Benjamin, New York, 1961); A. L. Fetter and J. D. Walecka, *Quantum Theory of Many-Particle Systems* (McGraw-Hill, New York, 1971); G. D. Mahan, *Many Particle Physics* (Plenum, New York, 1981).
- [42] V. Fock, Z. Phys. **47**, 446 (1928).
- [43] C. G. Darwin, Proc. Cambridge Philos. Soc. **27**, 86 (1930).
- [44] R.B. Dingle, Proc. Roy. Soc. (London) A **211**, 500 (1952).
- [45] L.J. Slater, *Confluent Hypergeometric functions* (Cambridge, London, 1960).
- [46] E.W. Hobson, *The Theory of Spherical and Ellipsoidal Harmonics* (Chelsea, New York, 1955).
- [47] H.A. Bethe and E.E. Salpeter, *Quantum Mechanics of One- and Two-Electron Atoms* (Academic Press, New York, 1957); See, e.g., the Appendix on Spherical Harmonics.
- [48] N.D. Mermin, Phys. Rev. B **1**, 2362 (1970).
- [49] M.S. Kushwaha and F. Garcia-Moliner, Phys. Lett. A **205**, 217 (1995).
- [50] J.D. Jackson, *Classical Electrodynamics* (John Wiley, New York, 1975).
- [51] R.C. Ashoori, Nature **379**, 413 (1996); R.J. Warburton *et al.*, Nature **405**, 926 (2000).
- [52] F.D.M. Haldane, Phys. Rev. Lett. **51**, 605 (1983).
- [53] J.K. Jain, *Composite Fermions* (Cambridge, New York, 2007).